ORIGINAL RESEARCH PAPER

The formation of the 8˚20′ N seamount chain, east pacific rise

Valentina Romano[1,2] · Patricia M. Gregg[1] · Yan Zhan[1,3] · Daniel J. Fornari[4] · Michael R. Perfit[5] · Dorsey Wanless[6] · Maurizio Battaglia[2] · Molly Anderson[5]

Abstract

Near-axis seamounts provide a unique setting to investigate three-dimensional mantle processes associated with the formation of new oceanic crust and lithosphere. Here, we investigate the characteristics and evolution of the 8˚20'N Seamount Chain, a lineament of seamounts that extends ~ 175 km west of the East Pacific Rise (EPR) axis, just north of the fracture zone of the Siqueiros Transform Fault. Shipboard gravity, magnetic, and bathymetric data acquired in 2016 are utilized to constrain models of seamount emplacement and evolution. Geophysical observations indicate that these seamounts formed during four distinct episodes of volcanism coinciding with changes in regional plate motion that are also reflected in the development of intra-transform spreading centers (ITSCs) along the Siqueiros transform fault (Fornari et al. 1989; Pockalny et al. 1997). Although volcanism is divided into distinct segments, the magnetic data indicate continuous volcanic construction over long portions of the chain. Crustal thickness variations along the chain up to 0.75 km increase eastward, inferred from gravity measurements, suggest that plate reorganization has considerably impacted melt distribution in the area surrounding the Siqueiros-EPR ridge transform intersection. This appears to have resulted in increased volcanism and the formation of the 8˚20'N Seamounts. These findings indicate that melting processes in the mantle and subsequently the formation of new oceanic crust and lithosphere are highly sensitive to tectonic stress changes in the vicinity of fast-spreading transform fault offsets.

Keywords Seamount volcanism · Marine gravity · Magnetics · Melt migration · East Pacific Rise

Introduction

Investigating processes associated with crustal formation and evolution at Mid-Ocean Ridges (MORs) is integral to understanding the creation and architecture of oceanic lithosphere. Near-axis seamount chains are unique settings for investigating crustal accretion at an adjacent ridge segment. The formation of near-axis seamounts, and their morphology and structural evolution can inform our understanding of the tectonic and melting processes occurring at nearby spreading centers. While some seamount lineaments are thought to be formed by hotspot-plate interaction due to their orientation being aligned with absolute plate motions (e.g., Lamont Seamounts: Fornari et al. 1984; Allan et al. 1989; Shen et al. 1993) (Fig. 1), or hotspot-ridge interaction (e.g., Galapagos Spreading Center: Mittelstaedt et al. 2012; Mittelstaedt et al. 2014), there are examples of intra-plate volcanic ridges comprised of chains of seamounts that may have been formed by structural processes unrelated to a hotspot source (Sandwell and Fialko 2004; Forsyth et al. 2006; Harmon et al. 2006; Cormier et al. 2011). These near-axis seamounts provide a particularly unique setting to investigate the interplay between tectonics and melting during the formation of new oceanic crust.

✉ Valentina Romano
    valentina.romano@uniroma1.it

[1] Department of Geology, University of Illinois at Urbana-Champaign, Champaign, IL, USA

[2] Now at Department of Earth Sciences, Sapienza University of Rome, Rome, Italy

[3] Now at Earth System Science Programme, The Chinese University of Hong Kong, Shatin NT, Hong Kong, SAR

[4] Geology and Geophysics Department, Woods Hole Oceanographic Institution, Woods Hole, MA, USA

[5] Department of Geological Sciences, University of Florida, Gainesville, FL, USA

[6] Department of Geosciences, Boise State University, Boise, ID, USA
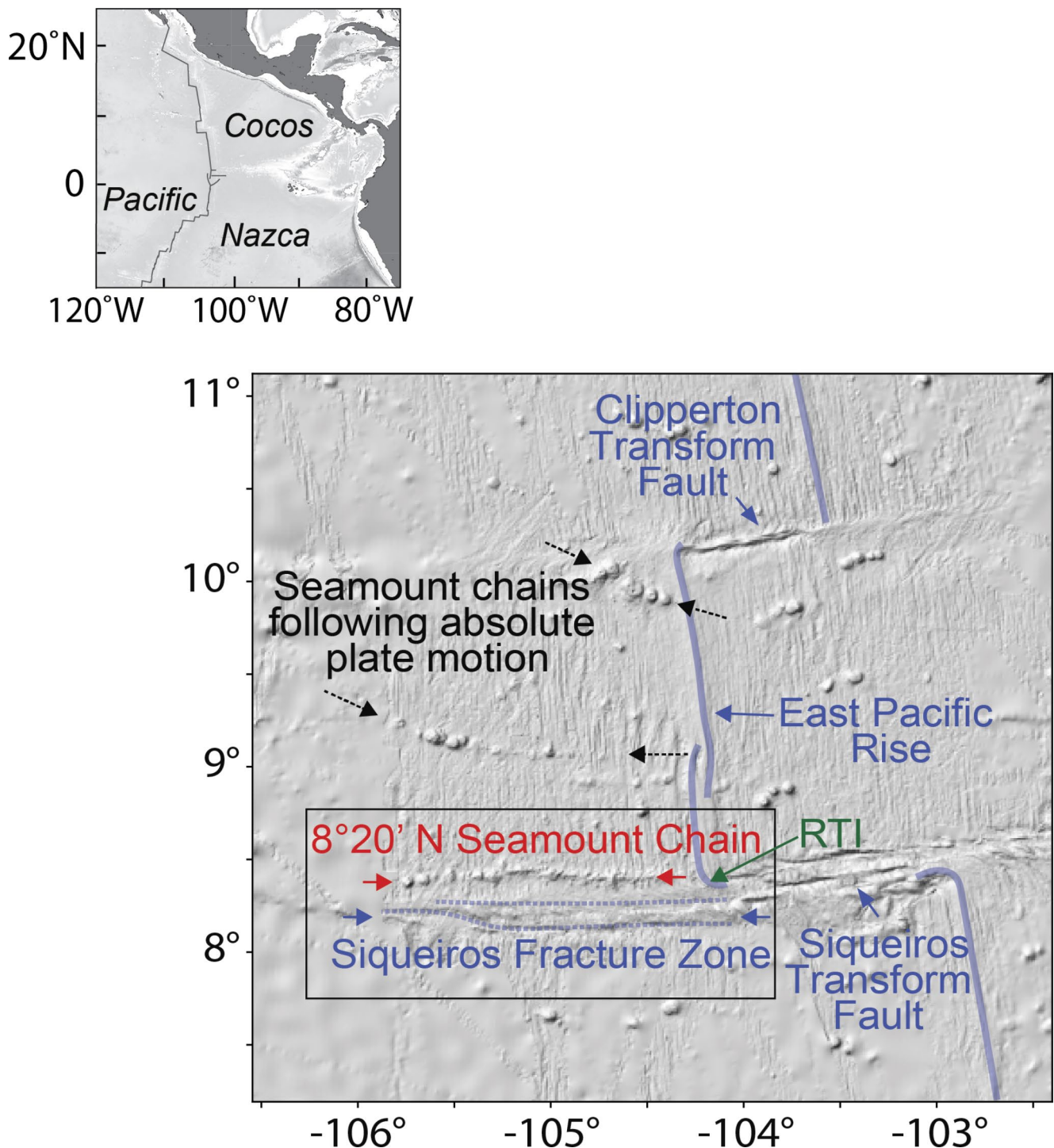
Fig. 1 Location of the study area is shown in inset as red square with the regional eastern Pacific plate boundaries. Dashed black arrows indicate example seamount chains that follow absolute plate motion. Siqueiros Transform Fault is located to the east of the Siqueiros Fracture Zone. The black box shows the location of the map shown in Fig. 2

The 8°20'N Seamount Chain extends west from the East Pacific Rise (EPR), north of the Siqueiros transform fault ridge-transform intersection (RTI), and is roughly parallel to the trend of the Siqueiros Fracture Zone to the south (Fig. 2). The chain consists of a ~ 175 km-long lineament of variably shaped volcanic constructs built on fast-spreading ocean crust (~ 109–121 mm/year full rate; Carbotte and Macdonald 1992) that spans an age range between ~ 0.05 to ~ 3 My. Rather than following the absolute plate motion trajectories of other seamount chains in the region, the orientation of the
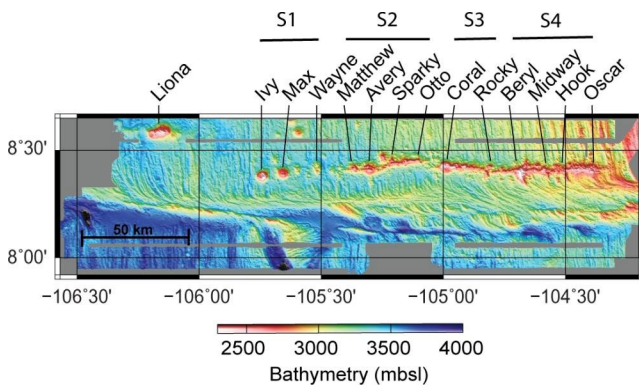
Fig. 2 Bathymetric map shows the 8°20'N Seamount Chain and names of key seamounts studied during the AT37-05 and AT42-06 cruises using RV *Atlantis* shipboard magnetics and gravity, and diving with *Alvin* and *Sentry*. S1, S2, S3 and S4 are the four recognizable segments in the 8° 20'N Seamount Chain, based on changes in its trend

8°20'N Seamounts is relative-motion parallel (Fig. 1). Several first-order tectonic plate readjustments have impacted the spreading geometry and segmentation of this portion of the EPR between 8–10°N, and the structural evolution of the Clipperton and Siqueiros transform faults (e.g., Perram and Macdonald 1990; Carbotte and Macdonald 1992; DeMets et al. 2010; Pockalny et al. 1997). Specifically, the 8–10°N EPR segment has undergone a series of counterclockwise plate motion reorganizations over the past 2–3 million years (Pockalny et al. 1997). The changes in plate motion have resulted in trans-tension and segmentation of the Siqueiros transform fault, leading to intra-transform spreading (Fornari et al. 1989; Perfit et al. 1996), and the generation of irregular topography both within and outside of the transform deformation zone (Pockalny et al. 1997). However, key questions remain about how plate motion reorganization has impacted crustal formation along the 9°-10°N segment of the EPR. The proximity of the 8°20'N Seamount Chain to the EPR-Siqueiros RTI and associated fracture zone may provide key clues about the evolution of this region of the EPR during the past ~ 3 million years.

Constraining the timing of seamount emplacement along the 8°20' N Seamount Chain, and whether volcanism was occurring coevally along the chain for specific periods of time are key to understanding the interplay between regional tectonic adjustments and mantle melting processes and how the lithosphere evolved on the west flank of the EPR in this area. In this study, new shipboard geophysical data are used to investigate the formation and evolution of the 8°20' N Seamount Chain. The present discussion focuses on the analysis of shipboard geophysical data (multibeam bathymetry, gravity, magnetic) and interpretation to determine inferred relative ages of seamount construction along the chain in comparison to the surrounding EPR-generated seafloor. The geophysical investigation provides insights on whether the seamounts comprising the chain formed coevally over large swaths of the off-axis terrain, or if the chain is an age progressive construct along its length. Additionally, the variations in crustal thickness in this region are investigated by gravity measurements and modeling.

Geologic background

Near axis seamounts in the 8°-10°N EPR region are numerous and groups of them have trends ranging from relative motion parallel to absolute motion parallel, and some appear to be a hybrid between both, likely reflecting plate readjustments as the seamounts formed (Macdonald et al. 1992; Allan et al. 1994; Batiza and Vanko 1984; Fornari et al. 1984; Niu and Batiza 1991, 1993; Scheirer and Macdonald 1995). The 8°20'N Seamount Chain is comprised of a series of volcanic centers and ridges aligned along several trends that are parallel to subparallel to the relative plate motion between the Siqueiros and Clipperton transform faults (Fig. 1). The overall strike of the 8°20'N Seamount Chain (269°) does not follow an absolute motion trend (283°) (De Mets et al., 2010) but appears to be more closely associated with the Pacific-Cocos relative plate motion trend (264°), and the trace of the western Siqueiros Fracture Zone (FZ) proximal to the Siqueiros-EPR RTI (Fig. 1; Table S2). Based on seafloor magnetic anomalies (Carbotte and Macdonald 1992) and satellite derived bathymetry (Smith and Sandwell 1997), slight changes in the seamount chain's trend are observed at ~ 2.5 Ma, 2 Ma, and 1.5 Ma, dividing the chain into four, recognizable segments (Fig. 2). Liona Seamount, the westernmost seamount, appears to be a separate volcanic construct. The most distal segment from the ridge axis (Segment 1) comprises the Ivy, Max, and Wayne seamounts. Segment 2 spans from Matthew to Otto Seamount. Segment 3 contains Coral Seamount and appears to end just east of Rocky Seamount. Finally, Segment 4, the most proximal, spans from just east of Rocky Seamount to Oscar Seamount, the most eastern portion of the chain, ~ 15 km from the EPR axis.

Carbotte and Macdonald (1992) and Scheirer and Macdonald (1995) cited the uniform high reflectivity recorded by sidescan sonar, and positive magnetic polarity to postulate coeval and relatively young formation of the 8°20'N Seamounts. Their findings suggested the potential for active volcanism at great distances from the EPR axis, and motivated our research to collect additional data along the chain to better resolve its geophysical and geochemical characteristics. Anderson et al. (2020) find that these seamounts are composed of highly heterogeneous MOR lava types originating from multiple mantle sources and variable degrees of mantle melting. The lava geochemistry and melting models

indicate 8°20'N seamount volcanism must occur away from the homogenizing effects of melt focusing and steady state magma chambers associated with the EPR axis, and therefore likely erupted at variable distances from the ridge axis (Anderson et al. 2020). It was postulated that regional plate motion changes may be responsible for the location and formation of the 8°20'N Seamount Chain (e.g., Scheirer and Macdonald 1995, and Pockalny et al. 1997). However linking the timing of plate reorganization to the formation and evolution of this seamount lineament is critical to understanding the evolution of the mantle and crustal accretion in this region.

Geophysical data collection

The shipboard geophysical surveying included the acquisition of coregistered multibeam, gravity, and magnetic data. Tie lines were collected along age isochrons to investigate the polarity of the seamount magnetization with respect to that of the surrounding crust. Those data provide a characterization of the Pacific plate north of Siqueiros FZ and a comparison with older lithosphere south of the Siqueiros FZ. Surveys were conducted at an average speed of ~10 knots with a sampling rate of ~1 Hz.

Multibeam data collection

Bathymetric data were collected in 2016, during the AT37-05 cruise, onboard the R/V Atlantis using a mounted Kongsberg EM122 multibeam system, with a swath angle of 65° in water ranging in depth from 4,251 to 2,029 m with corresponding swath widths of 5364-2,560 m. The survey consisted of eight E-W long survey lines (~200–225 km) and five N-S lines (~100 km), three of which transect the E-W survey (Figure S1). At the start of each long survey line, an 1800 m expendable bathythermograph (XBT) was launched to record sound velocity, conductivity, and temperature. XBTs do not measure salinity. The final, processed bathymetric data were gridded at 75 m in the WGS-84-UTM-13 N coordinate system.

The new EM122 multibeam data acquired reveals that the chain contains over 30 individual seamounts and elongate ridges comprised of coalesced edifices that range in elevation above the surrounding seafloor between 200 and 900 m; the shallowest summit depths range between 2100 and 2400 m, (200–400 m shallower than the ~2570 m depth of the adjacent EPR crest). While many of the seamounts at the western end of the chain have a circular plan-view morphologies with domed summits, the seamounts east of ~105°21'W (Matthew Seamount) appear to have coalesced

to form ridge-like structures (Fig. 2). Morphologically, the seamounts can be subdivided into 3 primary shape categories: circular volcanic morphology, volcanic lineaments parallel to the NNW-trending abyssal hill fabric, and ridge-like constructions trending perpendicular to the EPR axis. While Segment 1 is composed of single volcanic edifices, Segments 2 and 3 (60–120 km off-axis between Matthew and Rocky, Fig. 2) have coalesced into EPR-perpendicular ridges connecting circular seamount edifices. The edifices of Segment 4 are dominated by north-south trending ridge features that parallel the underlying abyssal hill fabric.

Magnetic data collection

Magnetic data (Fig. 5 A) were collected using a Marine Magnetics SeaSPY Overhauser Magnetometer System. Surveys were conducted with the magnetometer towed approximately 280 m behind the ship. Due to a "spark" effect thought to be caused by a cable issue, raw data were filtered using a 1000th median filter. Processing was performed using the NSF-supported Rolling Deck to Repository (R2R) Program code (Arko et al. 2011). The R2R code utilizes navigation information to generate the magnetic scalar potential at the time of the data collection and removed the corresponding IGRF model (Thébault et al. 2015) before outputting magnetic anomaly data.

Gravity data collection

Underway gravity data (Fig. 3 A) were collected using a BGM-3 marine gravimeter, installed on the R/V Atlantis to acquire continuous gravity data. Raw gravity data were filtered with a low-pass Butterworth filter and corrected for both Eötvös and drift correction. Land gravity ties were carried out at port stops in Newport, OR and Manzanillo, Mexico over the 3 months prior to the expedition, and were used to calculate the drift of the BGM-3 sensor to correct the data. The Free-Air Anomaly (FAA) was calculated by subtracting the corrected raw data with the IGF80 reference gravity field. The comparison of all the FAA data with the bathymetric maps acquired by the multibeam system ensured the consistency of the gravity data.

Data processing

Magnetic data processing

The calculated magnetic anomaly was combined with the multibeam bathymetric data to calculate the rock
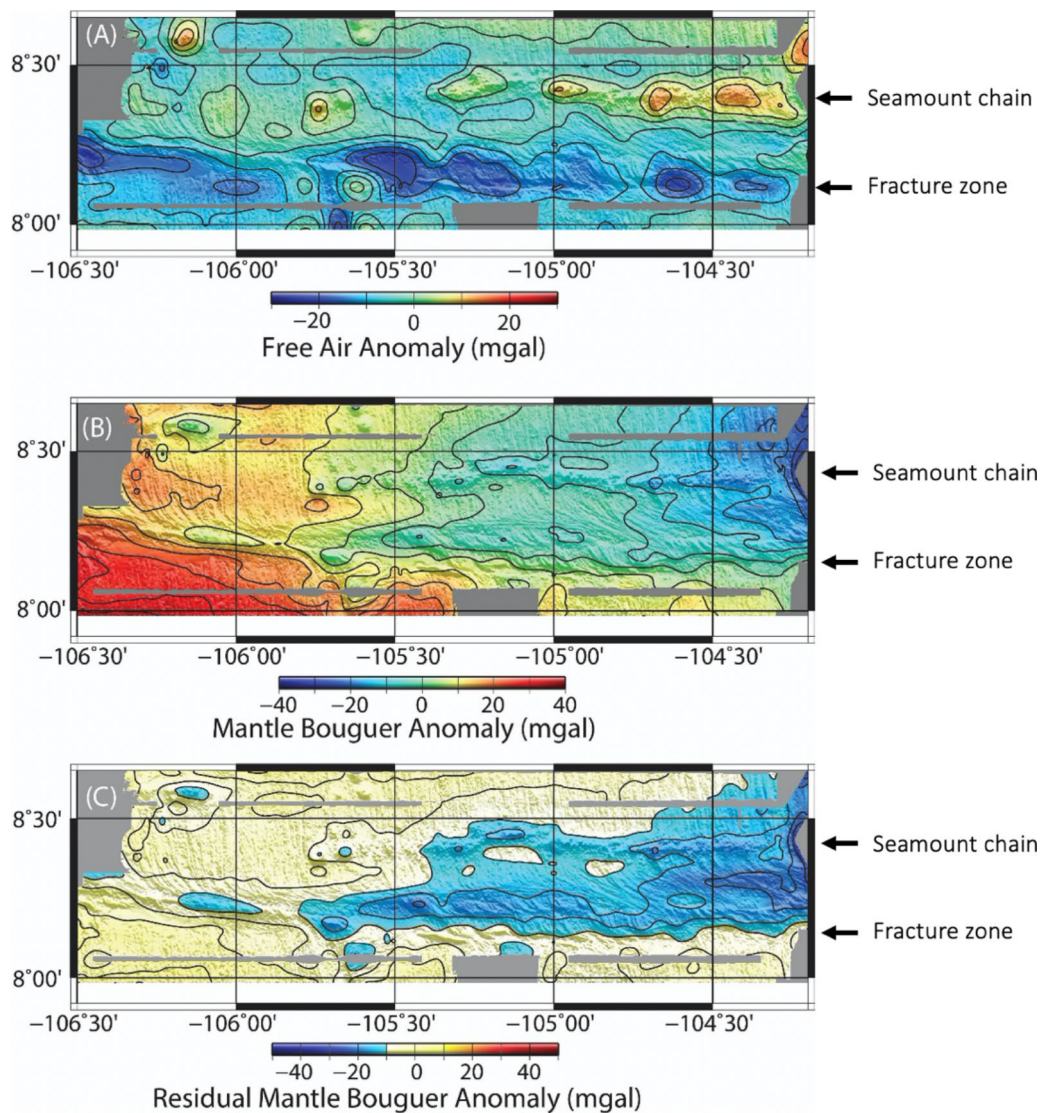
Fig. 3 A) Free Air Anomaly Map calculated filtering raw data using low-pass Butterworth filter and correcting for Eötvös and drift effects; B) Mantle Bouguer Anomaly map, calculated removing the effects of seafloor topography and a reference 6 km-thick crust. C) Residual Mantle Bouguer Anomaly is calculated by removing the effects of lithospheric cooling as estimated from a 3D passive mantle upwelling finite element model (see Fig. 4)

magnetization distribution in the study area. We followed the procedures described in Macdonald et al. (1980), and magnetic data processing previously reported by Hosford et al. (2003), Tivey (1994), Tivey and Johnson (1990) and Williams (2007). The data processing involved removing the effects of topography, revealing the distribution of crustal magnetization associated with the tectonic setting and the reversals in the polarity of the Earth's magnetic field through time, following the Fourier inversion method of Parker and Huestis (1974). A constant thickness source layer of 0.5 km was assumed, with the upper bound determined by the multibeam bathymetry grid. The layer was assumed to have a uniform magnetization oriented parallel to an axial geocentric dipole field. A bandpass filter to remove short and long wavelength features (4 and 800 km respectively) was applied. The 3D magnetization of the area was gridded at 0.25 km, using the same technique adopted for the gravity data. The new magnetic data and inversions are compared to the Carbotte and Macdonald (1992) and indicate a good agreement between the two approaches (Figure S2). Note that our goal is not to get a perfect fit between the AT37-05 and Carbotte and Macdonald (1992) inversions, but rather to illustrate that the approach we have used is comparable by being able to reproduce their 1992 inversion.

Fig. 4 Three-dimensional passive flow model used to simulate the thermal structure in the study area. Spreading velocities are imposed at the surface. Up is the velocity of the Pacific plate, Uc is the velocity of the Cocos plate. The temperature at the surface, T_0 and at the base, T_m are used as boundary conditions at the top and the base of the model box. The bottom and side boundaries are defined as stress free, allowing for convective flux of material into the model from below and out through the sides. The model is used to provide the temperature predictions for discrete horizontal layers at increasing depth
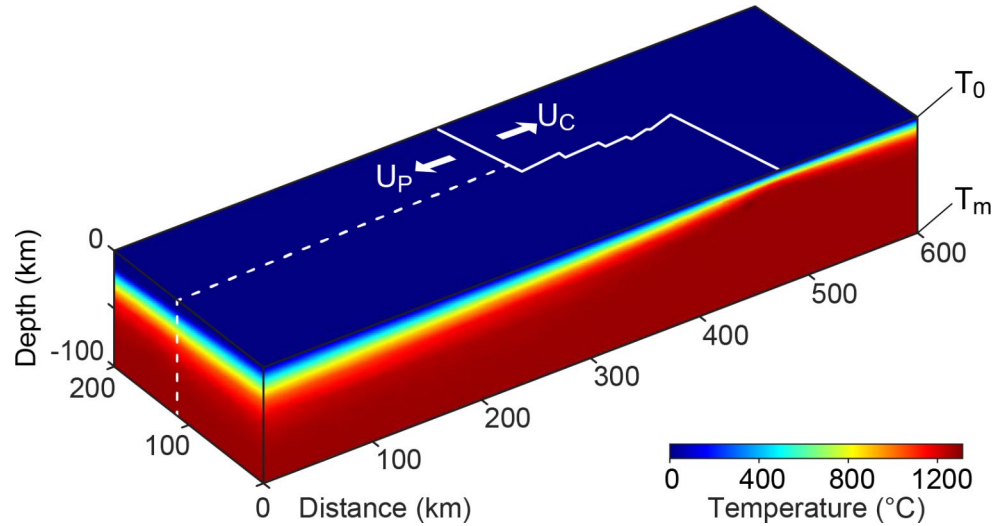
Gravity data processing

Using methods described in Kuo and Forsyth (1988), the Free Air Anomaly (FAA) was interpolated from gravity data onto a 0.25 km-spaced grid using a tension continuous curvature surface gridding algorithm (Fig. 3 A). We adopted the forward modeling approach of Kuo and Forsyth (1988) to separate effects of the different components contributing to the gravity signal (e.g., seafloor topography, Moho relief, and 3D mantle thermal structure). Parker's (1974) method was used to convert the elevation profile, from the multibeam data, and the density contrast to infer the gravity signal. For the water-crust interface, we assumed a density of 1.03 g/cm³ for the seawater and a density of 2.73 g/cm³ for the crust, and we assumed a constant crustal thickness of 6 km and a mantle density of 3.3 g/cm³ to estimate the attraction of the Moho (Gregg et al. 2007; Kuo and Forsyth 1988; Lin et al. 1990). We interpolated these data with the same criteria adopted for the FAA to generate the map of the Mantle Bouguer Anomalies (MBA; Fig. 3b). In a ridge-transform system, the density variations associated with lithospheric cooling are probably the dominant mantle source of the MBA (Kuo and Forsyth 1988; Lin and Phipps Morgan 1992), so a Residual Mantle Bouguer Anomaly (RMBA) was calculated to incorporate thermal subsidence (Kuo and Forsyth 1988), including heath loss due to hydrothermal circulation. The 3D upwelling mantle model described below, described in thermal model calculations below, provides the temperature predictions for discrete horizontal layers at increasing depths away from the ridge axis. Temperature was converted into density variations to provide the correction for the RMBA calculation (Fig. 3 A).

Thermal model calculations used for the RMBA

A three-dimensional (3D) passive mantle upwelling model was calculated using the commercial finite element software COMSOL Multiphysics® 5.3 (www.comsol.com), to evaluate the thermal structure in the region, following the methods of Gregg et al. (2009), in order to calculate the RMBA. The area of interest was focused on the region ~ 100 km North and South of the 8°20'N seamount chain (corresponding to ~ 9.2°N to 7.4°N); including the EPR axis and flanks, and the Siqueiros Transform Fault, including the four ITSCs within the transform. The geometry representing the ridge-transform-ridge system was defined within a computational domain 600 km long, 200 km wide and 100 km deep, large enough to encompass the study area (Fig. 4). Mantle flow is driven by the divergence of two plates, at the top of the domain, with a half spreading rate of 55 mm/yr. Surface temperature was assumed to be 0˚C and a mantle potential temperature of 1350 ˚C (Gregg et al., 2007, 2009) was imposed at the base of the model (see Table S1 for parameter values). The bottom and side boundaries were imposed as stress free, allowing for convective flux from the mantle below. We defined a tetrahedral mesh, which is finer in the first 30 km of depth and around plate boundaries.

The steady-state flow field coupled with temperature are controlled by conservation of mass, momentum, and energy, which is given by:

$$\nabla \bullet V = 0 \tag{1}$$

$$\nabla P = \nabla \bullet \left[\eta \left(\nabla V + (\nabla V)^T \right) \right] \tag{2}$$

$$\rho C_p \left(V \bullet \nabla \right) T = \nabla \bullet \left(t_k \nabla T \right) \tag{3}$$

Respectively, ρ is the density of the mantle, P is pressure, V is the velocity field, η is the effective mantle viscosity, C_p is the heat capacity, T is temperature, and k is the thermal conductivity.

We adopted a temperature dependent viscosity:

$$\eta_T = \eta_0 exp \left[\frac{Q}{R} \left(\frac{1}{T} - \frac{1}{T_m} \right) \right] \qquad (4)$$

where is the reference viscosity, Q is the activation energy, and R is the universal gas constant.

Gravity-derived elastic plate thickness model

The response of the oceanic lithosphere to an applied load (e.g., a seamount) is related to its rigidity and hence is tied to its age and thermal structure (Koppers and Watts 2010). The flexural rigidity of a plate can be related to the thickness of an elastic plate (Te) whose flexural properties approximate those of the oceanic lithosphere. Because the elastic thickness of the lithosphere represents its strength at the time of emplacement of the load, it can be used to estimate the age of the lithosphere at the time of loading (Watts 1978). Gravity anomalies are a sensitive indicator of the flexural properties of the lithosphere and are used along with bathymetric data to study the emplacement history of submarine volcanoes, such as the Hawaiian-Emperor chain (Watts 2001). Although this approach is problematic for near ridge volcanic constructions, we test whether there is an observable flexural response due to the loading of the 8°20' N Seamounts. In the Fourier transform domain, the relationship between the topography, gravity, and the gravitational admittance is given by (Watts 1978, 2001):

$$Z(k) = \frac{output}{input} = \frac{\Delta g(k)}{H(k)} \qquad (5)$$

where $Z(k)$ is the gravitational admittance, $\Delta g(k)$ are the discrete Fourier transform of the observed FAA and the topography, k is the wavenumber (2π/wavelength).

The ship observed FAA is used in combination with the multibeam bathymetric data to determine the relative differences in elastic plate thickness at the time of emplacement for portions of the 8° 20'N Seamount Chain (Table S2). The estimations of elastic plate thickness are subsequently used to infer the age of the lithosphere at the time of loading due to seamount formation. The elastic thickness is calculated for different profiles along the chain over the main seamount edifices following the approach by Watts (1978), where the gravitational admittance is given by:

$$Z(k)_{flex} = 2\pi G(\rho_l - \rho_w)e^{-kd} \left\{ 1 - \phi'_e(k) \frac{((\rho_c) + (\rho_m - \rho_c)e^{-kt})}{(\rho_m)} \right\} \qquad (6)$$

where $\phi'_e(k) = \left[\frac{Dk^4}{(\rho_m - \rho_c)g} + 1 \right]^{-1}$, G is the gravitational constant, ρ_l is the density of the load, ρ_w is the density of the water, ρ_c is the density of the crust, is the density of the mantle, d is the mean water depth, t is the mean thickness of the crust, D is the flexural rigidity:

$$D = \frac{ET_e^3}{12(1 - \nu^2)} \qquad (7)$$

where E is the Young's modulus and v is the Poisson's ratio and Te is the elastic thickness.

The shipboard gravity data are compared directly with the theoretical gravity anomalies computed through Eqs. 5–6, for different values of the Te, using the observed bathymetry. The other parameters are maintained fixed at the values reported in Table S2. Te estimates were calculated along profiles running N-S and crossing the volcanic edifices to investigate variations associated with the seamount chain given their location at specific distances from the EPR axis.

Uncertainties in Te can be related first to the source data in terms of positioning errors and measurement errors. Thanks to the high accuracy and resolution of the acquired bathymetric data as well as the Global navigation satellite system (GNSS) navigation, the associated errors in the calculations of the elastic thickness can be considered negligible. Other uncertainties associated with the parameters and assumptions used for the calculation (e.g., density, see Eq. 6) can be considered of the same order of magnitude of the observed gravity data. The application of this method for the 8°20'N Seamount Chain is challenging because of three effects: the presence of the fracture zone to the south, which limits our ability to fit the results in the southern portions of the analyzed profiles, the proximity of the study area to the EPR ridge axis, and the Watts (2001) one-dimensional approach assumes a large, central edifice structure and may not adequately describe the flexural compensation of linear, coalesced features. For this reason, the elastic plate thickness values were fitted along the profiles running north of the seamount to avoid the fracture zone to the south and we have focused our calculations on the largest edifices.

Results

The inverted three-dimensional magnetization indicates the seamount lavas have recorded a series of magnetic reversals along the chain (Fig. 5). However, the eastern portion of the chain (east of 105°W) exhibits normal polarity in agreement with previous findings (Carbotte and Macdonald 1992; Figure S2). If the seamounts are age progressive, forming nearer to the ridge axis than their current location,
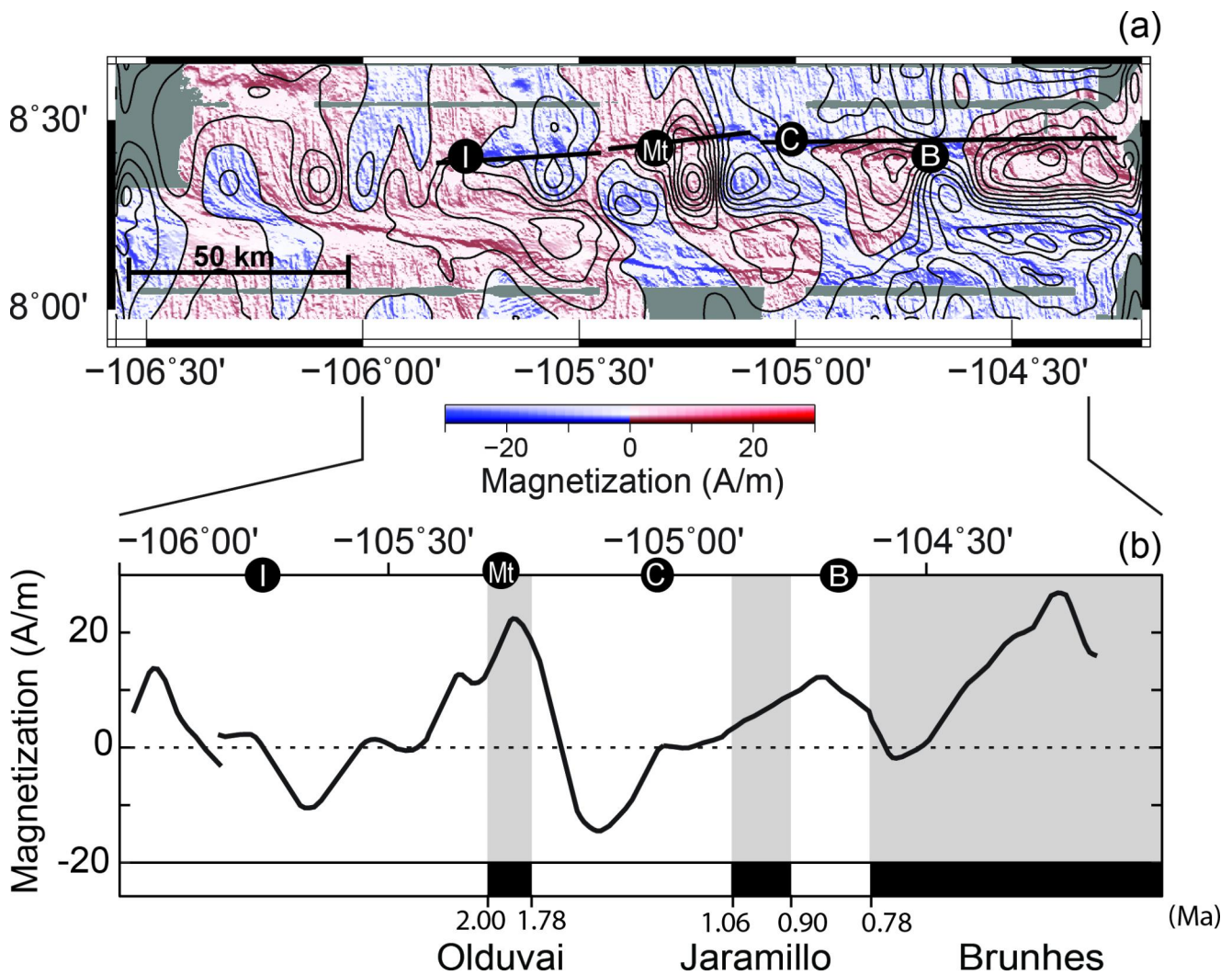
Fig. 5 (a) Inverted 3-dimensional magnetization. Red colors indicate positive, normal polarity and blue colors are indicative of negative, reverse polarity. The black line denotes the profile shown in (b). (b) Seamount magnetization (black line) taken along the edifices of the 8°20'N seamounts chain as illustrated by the white line in (a). The black bars and gray shading indicate normal/positive polarity and white bars indicate reverse polarization according to the magnetization of the seafloor in the 8°-8.5°N region (Carbotte and Macdonald 1992). I = Ivy, Mt = Matthew, C = Coral, B = Beryl

their magnetic reversals should mostly correlate with those recorded by the crust on which they were emplaced. A two-dimensional profile was extracted across the seamount chain to investigate the polarity of the seamounts in comparison to that of the surrounding crust (Fig. 5b). Overall, the magnetization recorded by the seamounts mimics the reversals in polarity recorded in the surrounding seafloor. However, the deviation in polarity along portions of the chain between −105°W and −104°40' W indicates that the seamounts are younger than the seafloor surrounding the edifices, as also suggested by previous investigations (Carbotte and Macdonald 1992; Scheirer and Macdonald 1995). This finding indicates that volcanism continued up to, and potentially beyond, 100 km from the ridge axis, well outside the region normally thought to be related to EPR axis-focused volcanic

activity (i.e., 5–10 km from the ridge axis; Carbotte et al. 2012). Three-dimensional seismic studies clearly illustrate the formation of off-axis melt lenses 2–10 km from the ridge axis (e.g., Perfit and Chadwick 1998; Canales et al. 2012; Han et al. 2014: Aghaei et al. 2017). However, given the location of the eastern-most seamounts of the 8°20'N Seamounts, it appears that they begin to form at least 15 km from the ridge axis.

Gravity data are utilized to produce a residual mantle bouguer anomaly (RMBA) along the 8° 20'N Seamount Chain following the approach of Kuo and Forsyth (1988; see Fig. 3 C). The RMBA calculation is inverted, assuming a constant crustal density structure, to estimate the crustal thickness variations needed to reproduce the observed signal (Fig. 6). Crustal thickness variations along the seamount
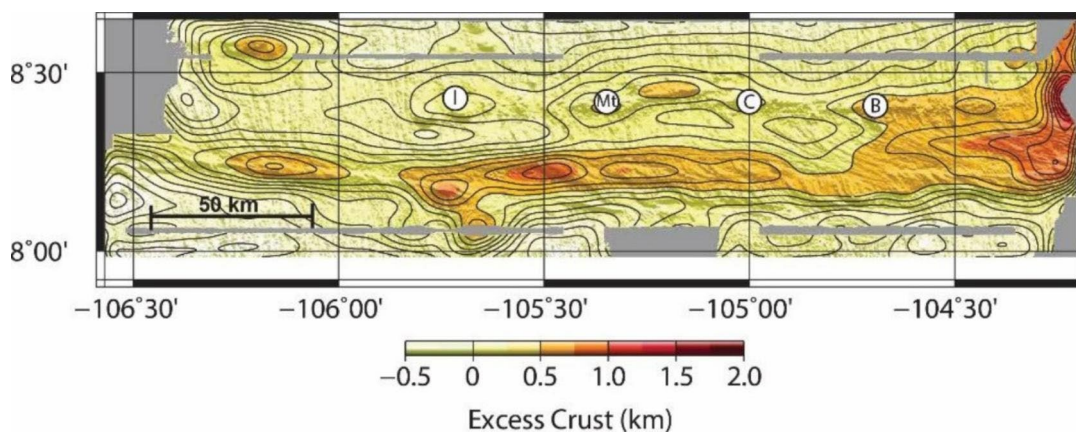
Fig. 6 Map of crustal thickness variation on the west flank of the EPR in the area adjacent to the 8˚20'N seamount chain. Anomalous crustal thickness variations are in the range of 0.5 to 1 km. While direct calculations of error are not available, given the error range of the FAA observations and multibeam data, RMBA likely reflects errors of 5–10%. The map indicates an increase in crustal production toward the ridge axis, located at ~ 104˚12' W. I = Ivy, Mt = Matthew, C = Coral, B = Beryl
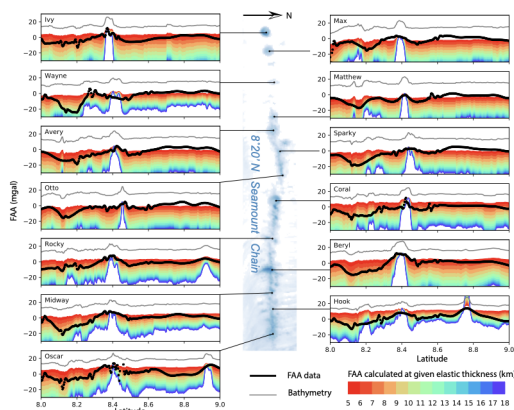

Fig. 7 Using Watts et al. (1978), *Te* estimates are calculated for all of the major edifices observed along the seamount chain, along N-S profiles that cross each seamount summit. Best fit estimations for each seamount are shown with bold lines, bathymetry is indicated by the grey line. Model predictions for Matthew and Beryl give similar *Te* estimates suggesting that Matthew may have formed further to the east. Coral's relatively high *Te* value may indicate that it has formed in place at ~ 105°W. Each profile is disrupted to the south by the Siqueiros Fracture Zone, as such, the best model fit to the FAA was found by comparing the values to the north of the chain. In the center of the figure we have included a gray shaded map of the seamounts, however for details, please refer to Fig. 2

chain indicate an increase eastward towards the EPR axis, with the greatest crustal thicknesses (~ 6.5 to 7 km) found east of 104°45'W. Quantifying the absolute errors is difficult; however, the sensitivity of the instrumentation plus the potential errors introduced during processing likely results in < 0.5 mgals of error. Although this modest thickness increase is comparable to variations of average fast-spreading crustal thicknesses (e.g., ~ 5.5–6.5 km; Canales et al. 2003: Aghaei et al. 2014), the increases are significant compared to the crust surrounding the seamount chain to the North. It is important to also note that gravity observations are much more sensitive to variations in the extrusive layer thickness and may not capture significant increases within the plutonic layer (Gregg et al. 2007). As such, the observed increase in crustal thickness is likely underestimated.

Several edifices with well-defined bathymetric highs were chosen along the chain for *Te* analysis (Fig. 7). Seamounts Ivy, Max, Matthew, Avery, and Coral all exhibit round, pancake-shaped edifice morphologies, whereas the summits of Beryl and Rocky seamounts are linear, paralleling the seafloor abyssal hill fabric. We find that the critical feature of Watts' (2001) approach is the size of the edifice relative to its surroundings. If an edifice is too close to another large feature, such as another seamount or a fracture zone, or has coalesced with nearby seamounts, it will not provide an adequate *Te* model result for the elastic plate thickness (e.g., Hook, Oscar, Rocky, Wayne, and Sparky in Fig. 7). The eastern portion of the 8 20°N seamount chain is composed of coalesced seamounts forming linear and sublinear ridges. In many cases these seamounts do not exhibit a large central edifice needed for an adequate estimation of *Te*. For example, in Segment 4 the edifices are dominated by north-south ridge features that parallel the abyssal hill fabric of the seafloor (Fig. 2). As such, while we have applied the modeling approach along the entire seamount chain, many of the coalesced seamounts (Fig. 7 and square symbols in Fig. 8) do not provide good targets for this modeling approach.

A comparison of the estimates of *Te* with predicted current elastic plate thicknesses according to a cooling thermal model (Gregg et al. 2009; see Sect. 4.2; Fig. 4), supports the conclusion that not all of the seamounts formed near their current geographic locations. Since *Te* represents the
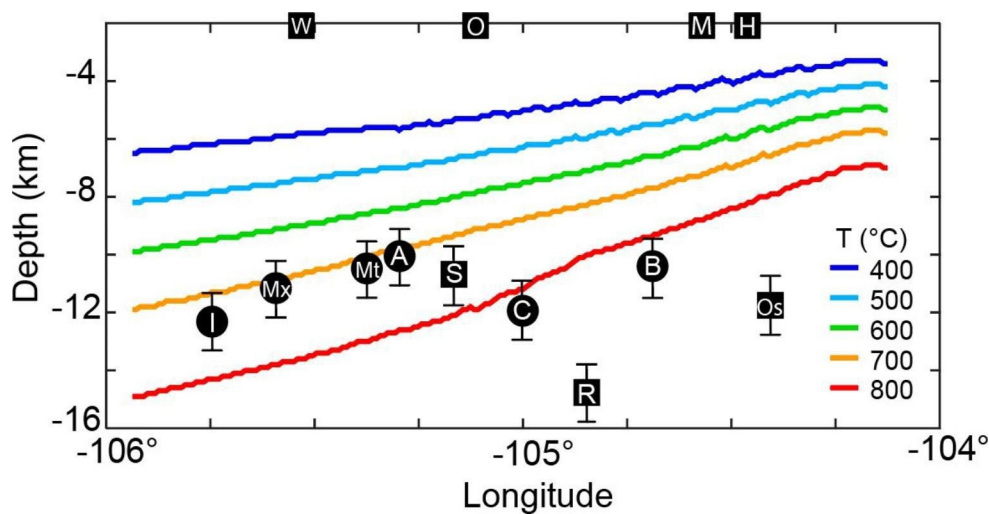
Fig. 8 The 400 °C to 800 °C isotherms are plotted from a profile extracted from the 3D thermal model (Fig. 4) along the 8°20'N seamounts chain to provide potential elastic thicknesses (*Te*) if the seamounts formed at their current locations. Capital letters indicate the seamounts: I = Ivy, Mx = Max, W = Wayne, Mt = Matthew, A = Avery, S = Sparky, O = Otto, Cr = Coral Ridge, C = Coral, R = Rocky, B = Beryl, M = Midway, H = Hook, Os = Oscar. The black circles (large edifices) and the black squares (coalesced seamounts forming linear ridges) indicate modeled *Te* (see for comparison Fig. 7 and Table S2). If the seamounts all formed close to the ridge the estimated *Te* would not parallel the predicted isotherms. Coalesced seamounts forming linear ridges (black squares) in many cases did not provide an adequate model result (e.g., W, O, Cr, M, H; see for comparison Fig. 7 for details)
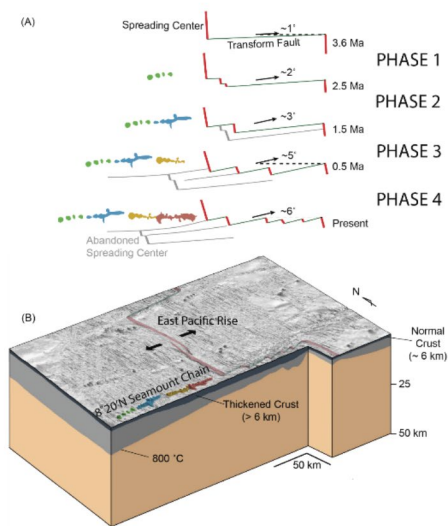
elastic thickness of the plate at the time of bulk emplacement of the edifice, if all of the seamounts formed at or near their present locations the estimated *Te* for the seamounts should parallel isotherms representing the base of the elastic plate. The 600 °C isotherm is typically assumed to be the temperature of the brittle-ductile transition in the oceanic lithosphere (McKenzie et al. 2005); however, the 800 °C isotherm, appears to provide a better fit to our data. In Fig. 8, for example, the portion of the chain containing the edifices from Ivy to Avery appears to be related to the 700 °C isotherm indicating that if they formed in situ the elastic plate would be defined by 700 °C. However, Coral and Beryl appear to parallel the 800 °C isotherm and cannot be explained with an elastic plate defined by 700 °C. However, that the isotherms are model specific and are used only for relative comparison. The important result from this exercise is the relative comparison of *Te* between adjacent seamounts and along specific segments of the chain. For example, if the minimum *Te* during the formation of Beryl and Coral Seamounts is 11 and 12 km respectively, then Ivy and Matthew Seamounts, which exhibit *Te*'s of 13 km and 11 km respectively, likely formed closer to the ridge axis than their current locations. One possibility is that if Beryl and Coral formed in situ, Matthew seamount formed near Beryl's location and was subsequently rafted westward ~ 75 km to its current position. Similarly, Ivy Seamount may have been originally emplacement close to Coral's current location and has since been rafted west ~ 60 km to its current position. From this perspective, we can assume the trend drawn by Coral's and Beryl's *Te* values (Fig. 8) to

be representative of the isotherm bounding the base of the elastic plate in this region.

Discussion

Building the 8°20'N seamount chain – temporal evolution and tectonic links

Gravity, magnetics, and bathymetric data analysis and modeling indicate that the 8°20'N Seamount Chain exhibits both coeval and age progressive volcanism, with episodic formation of seamounts in different sections of the chain. This is perhaps best illustrated by comparing the *Te* values estimated for Coral and Beryl Seamounts with those from Ivy and Matthew Seamounts (Fig. 8) and combining this with the observed magnetization profile along the chain (Fig. 5b). Coral and Beryl lie along the same isotherm (800 °C) and have the same elastic thicknesses as Matthew and Ivy (~ 13 and 12 km respectively). Additionally, Coral, Matthew, and Ivy Seamounts exhibit magnetization that is oppositely polarized to the adjacent seafloor upon which they were constructed. This suggests that the seamounts in Segment 3 from Coral to Beryl may have formed coevally. Similarly, the trend observed in *Te* in Segments 1 and 2 from Avery to Ivy may be indicative of coeval formation (Fig. 8). If these seamounts had formed in an age progressive fashion, such a strong trend should not be observed in the *Te*. Thus, we suggest that sections of the chain may have formed relatively

of melts, eventually leading to excess melting and volcanism in the region surrounding the western Siqueiros-EPR ridge-transform intersection (RTI). That said, when searching the seafloor for similar features at segmented transforms that have undergone similar trans-tension and segmentation, they are not ubiquitous features. For example, no such constructs are visible at Gofar, Quebrada, Discovery, Yaquina, or Garrett transform faults along the southern EPR. While the Wilkes Transform Fault (located at ~9°S) has several nearby seamount chains, they do not appear to span as far off-axis nor align so closely with the flanking fracture zones. An additional process such as an above average melt supply due to ridge migration (e.g., Carbotte et al. 2004) may be necessary to sustain volcanic construction off-axis. Regardless, it appears that the timing of the discrete changes in plate motions and the emplacement of the 8° 20'N Seamount Chain are intrinsically linked.

We suggest that the segments of the 8°20'N Seamount Chain initiated during four distinct phases and that these phases correlate with the changing plate geometry observed along 8°-10°N EPR over the past ~3 Ma (Pockalny et al. 1997; Fig. 9). While the seamounts appear to have initiated in these distinct groups, geochemical observations indicate that volcanism was continuous throughout the 3 My (Anderson et al. 2020).

- Phase 1: ~3 Ma to 2 Ma. The initial stage of volcanism that formed part of the 8° 20'N chain included growth of Max, Ivy, and Wayne seamounts as individual edifices, forming coevally ~50–75 km from the EPR ridge axis. These seamounts make up Segment 1 (Fig. 2).
- Phase 2: ~2 Ma to 1.5 Ma. The initiation of Segment 2 of the 8°20'N Chain. Matthew and Avery seamounts display a morphologic change from individual edifices to composite, coalesced seamounts. The shift in the chain's morphology is also manifested in an increase in gravity derived crustal thickness of ~0.5 km. If crustal thickness variations are an indication of melt production, the increase of crustal thickness along the seamounts formed during Phase 2 may indicate an increase in melt supply to the system as compared to Phase 1. Matthew Seamount to Otto Ridge, appear to have formed between ~30–50 km closer to the EPR crest and were rafted off to their current position, as indicated by the *Te* value of Matthew, that is similar to that of Beryl's at its current location.
- Phase 3: ~1.5 Ma to 0.5 Ma. This phase of volcanism initiated the seamounts from Coral to Beryl, Segment 3. The volcanism during Phase 3 created a continuous volcanic ridge flanked by Coral Seamount to the west and Beryl Seamount to the east. *Te* estimates suggest that

Fig. 9 A) The seamounts are shown in context with plate reorganization during the past 3.6 Myr. The red lines show the trace of the EPR and intra-transform spreading centers of the Siqueiros Transform Fault (grey lines). The black arrows indicate the degree of rotation of the plates at each time step. (adapted from Pockalny et al. 1997). The active seamounts corresponding to the age of the crust on which they were emplaced are shown for each time step in colors. Green represents seamounts of Phase 1, blue = Phase 2, yellow = Phase 3, and the most recent constructions are dark red for Phase 4. B) Three-dimensional illustration showing the bathymetry (shaded gray), the seamount locations (same color scheme as in a), the trace of the EPR (pink), Clipperton and Siqueiros Transforms (green) and the trend of the 800 °C isotherm

coevally, but the entire chain was not built within one specific period (Fabbrizzi et al. 2022, accepted).

The Siqueiros FZ exhibits a complicated history, marked by four plate reorganization events at ~3.6 Ma, 2.5 Ma, 1.5 Ma and 0.5 Ma (Pockanly et al. 1997). The correlation of our geophysical results with plate motion reconstructions for the Siqueiros – EPR plate boundary, suggests that the formation of the 8°20'N seamounts is related to the tectonic evolution of the Siqueiros transform for the past ~3 My (Fig. 9), as is also hypothesized by previous plate reconstruction models (Pockalny et al. 1991, 1997). It is likely that the processes associated with intra-transform spreading within the Siqueiros transform may have redirected mantle flow towards the transform fault and fracture zone (e.g., Gregg et al. 2012). This could have directly impacted the focusing

Coral and Beryl formed at or near their current location, ~ 60–90 km from the EPR ridge axis.

- Phase 4: ~0.5 Ma to present. The easternmost seamounts in the chain, Segment 4, east of Beryl to Oscar, are younger volcanic constructs that likely formed at their present locations. Elastic plate thickness calculations for this region are problematic due to the lack of large edifices and the proximity to the EPR ridge axis. However, the positive magnetic polarity observed along most of this portion of the seamount chain indicates volcanism younger than the Brunhes reversal (~ 780 ka).

Magnetic records and geochemical observations

Gravity data indicates how the volcanic segments of the 8°20'N seamount chain initiated in four distinct phases corresponding to four plate reorganization events (Pockanly et al. 1997). On the other hand, magnetic data suggests that volcanism continues for long periods after the initial formation of the seamounts. Combined, these observations suggest that although the onset of each of the segments of the seamount chain is marked by four different phases, the seamounts are long-lived features, with continuous activity beyond their initial location of formation. The geochemical variability observed from lavas collected along the 8°20'N chain support this line of thought (Anderson et al. 2020). Geochemical models suggest in fact that the 8°20' N seamount chain formed from variable extents of melting of a heterogeneous mantle that spans the range of compositions inferred to exist in the northern EPR region. The large range of basalt compositions present along the chain as well as their proximity to each other is inconsistent with magmas evolving in well-mixed magma chambers (e.g., EPR) and instead points to independent plumbing systems separated from the on-axis system to avoid mixing and homogenization.

Elastic plate thickness and lithosphere evolution

The modeled elastic plate thickness along the 8°20'N Seamount Chain provides additional insights into the evolution of the oceanic lithosphere and its rheological behavior in the near ridge environment. Since the maximum depth of intraplate earthquakes and the effective elastic thickness correlate with the age of the lithosphere, it is hypothesized that the main factor controlling plate strength and the evolution of the oceanic lithosphere is likely temperature (Chen and Molnar 1983; Wiens and Stein 1983; McNutt 1984; Stein and Stein 1992). This rheological control is manifested in the bathymetric subsidence of the plate as it ages (Stein and Stein 1992) and how the plate deforms in response to applied loads such as the construction and evolution of

seamounts, ocean islands, fracture zones, and subduction zones (Watts et al., 1978; Searle and Escartín 2004). Classic rheological models and temperature estimates derived from flexural studies predict that the 600 °C isotherm is the temperature of the brittle-ductile transition in the oceanic lithosphere (Parson and Sclater 1977; Minshull and Charvis 2001; McKenzie et al. 2005). However, lithospheric thickness may also be estimated seismically, for example by modeling surface-wave dispersion. Such methods yield lithospheric thickness estimates that are larger than those estimated from flexural studies, fitting closer to the 1000 °C isotherm (Leeds et al. 1974; Nishimura and Forsyth 1989). The calculated elastic thickness values (Table S2) along the 8°20'N Seamount Chain indicate that the 600 °C isotherm may not be an appropriate estimate for the brittle-ductile transition in this near-ridge axis setting. If the seamounts formed near the ridge and were subsequently rafted away to their current position, the elastic plate thickness at the time of loading should appear much thinner than the thickness of the lithosphere at their current location (Koppers and Watts 2010). Instead, if the seamounts formed at their present location, their elastic thicknesses should conform to the current lithospheric thickness, which we have estimated from the 3D thermal model (Fig. 4). Given these results, we find that the brittle-ductile transition may occur around 700 ~ 800 °C for the seamount chain between Ivy and Sparky (Fig. 8). Estimates of the thermal regime controlling elastic plate thickness in fracture zone settings indicate isotherms higher than 600 °C may govern the boundary of the elastic plate due to thermal bending and differential subsidence (Sandwell and Schubert 1982; Sandwell 1984; Parmentier and Haxby 1986; Wessel and Haxby 1990). In fact, although commonly used rheological models can capture first order processes taking place in the lithosphere, many key elements are not considered - e.g., the three-dimensionality of tectonic structures near ridge discontinuities and many models are two dimensional (Searle and Escartín 2004). We believe that the complexity of the 8°20'N seamount region, due to the presence of the nearby fracture zone, may have impacted the rheology of the oceanic lithosphere.

While our results indicate that the 800 °C isotherm likely controls the elastic plate thickness on the west flank of the EPR north of the Siqueiros FZ, thermal models of oceanic lithosphere may vary due to the assumed rheology, model parameters, and boundary conditions used during model setup and implementation. The robustness of the thermal model presented here can be evaluated by how well the estimates of thermal subsidence match the regional observations as illustrated by the RMBA (Fig. 3c). The RMBA map (Fig. 3c), obtained by subtracting the regional mantle thermal structure, shows a good correlation with the structural units and the residual anomalies following the strike of the

seamount chain and the fracture zone. This result indicates that the thermal subsidence has been effectively removed from the MBA and that the thermal model has provided an adequate estimation of the cooling of the lithosphere in this region.

The 8° 20'N seamount region illustrates how, when investigating complex tectonic settings, more sophisticated modeling approaches are necessary. Classic models that do not account for the three-dimensional thermal structure (i.e., proximity to a fracture zone and ridge) may not adequately reproduce the evolution of the elastic plate thickness. While the 1-dimensional approach of Watts (2001) works well for single, circular edifices, it is inadequate to estimate elastic plate thicknesses for volcanic constructs that have three-dimensional morphological variations, such as seamounts that are linear or coalesced. The inconsistency between the general trend of modeled effective elastic thickness and typical isotherms from this study and previous studies (e.g., Gregg et al. 2007; 2012) indicates the insufficiency of current elastic plate models. The 1-dimensional estimation of elastic thickness overlooks the possible variations in rock stiffness due to fracturing, alteration, and different compositions. Given the excess volcanism and crustal thickness values, there is every indication that the lithosphere near the RTI is indeed warm and that the 800-degree isotherm may in fact be appropriate.

Conclusion

Geophysical observations indicate that the 8°20'N Seamount Chain likely resulted from continuous volcanism that produced a chain punctuated by distinct variations due to regional tectonics. In particular, the four volcanic segments of the 8°20'N Seamount Chain appear to be age progressive, likely initiating in four phases coinciding with plate motion reorganizations (Pockalny 1997). The seamounts of Segment 4, east of ~ 105°W (~ 15–100 km from the EPR axis), exhibit young, potentially current, volcanism. Although punctuated by four distinct phases of volcanic initiation, magnetization recorded along the 8°20'N Seamount Chain suggests that the volcanism is long-lived and continues well past the location of initial seamount formation and flexural loading. Excess crustal thickness variations of ~ 0.5 to 1 km suggest an increase in crustal production eastward along the chain, that coincides with larger volcanic edifices observed east of -105°20' W (~ 125 km from the ridge axis). The increase in estimated crustal thicknesses corresponds with lithosphere younger than 2 Myr and an observed morphological change in the seamount chain from individual edifices to the west in Segment 1 to a linear ridge of coalesced seamounts east, Segments 2–4. These findings

have important implications for melt generation and transport processes at fast spreading MORs. Specifically, the interplay between tectonics controlled by cooling and fracturing of oceanic lithosphere proximal to a transform fault that has experienced a complex structural history and magmatism at great distances from the spreading axis suggests that melting and crustal construction can occur at much greater distances from the axis than previously inferred. Elastic plate thickness estimates for the 8°20'N seamount region illustrates how, when investigating complex tectonic settings, more sophisticated modeling approaches that account for the three-dimensional thermal structure are necessary. Ultimately, the implications of this work relate to the availability of melt at great distances from the accretionary plate boundary (e.g., Klein and Langmuir 1987; Langmuir and Forsyth 2007), how melt availability may vary through time, the interplay between off-axis volcanism and regional plate tectonics, and the evolution of the oceanic lithosphere.

Ethics declarations

Conflict of interest The authors declare no conflict of interest.

References

Aghaei O, Nedimović MR, Carton H, Carbotte SM, Canales JP, Mutter JC (2014) Crustal ckness and Moho character of the fast spreading East Pacific Rise from 9 420 N to 9 570 N from post stack-migrated 3D MCS data. Geochem Geophys Geosyst 15:634–657. https://doi.org/10.1002/2013GC005069

Aghaei O, Nedimovic MR, Marjanovic M, Carbotte SM, Pablo Canales J, Carton H, Nikic N (2017) Constraints on melt content of offaxis magma lenses at the East Pacific Rise from analysis of 3-D seismic amplitude variation with angle of incidence. J Geophys Research: Solid Earth 122:4123–4142. https://doi.org/10.1002/2016JB013785

Allan JF, Batiza R, Sack RO (1994) Geochemical characteristics of Cocos Plate seamount lavas. Contrib Miner Petrol 116:47–61. https://doi.org/10.1007/BF00310689

Allan JF, Batiza R, Perfit MR et al (1989) Petrology of Lavas from the Lamont Seamount Chain and Adjacent East Pacific Rise, 10 N. J Petrol 30:1245–1298. https://doi.org/10.1093/petrology/30.5.1245

Anderson M, Wanless VD, Perfit M, Conrad E, Gregg P, Fornari D, Ridley WI (2020) Extreme mantle heterogeneity in mid-ocean ridge mantle revealed in lavas from the 8°20' near-axis seamount chain. Geochemistry, Geophysics, Geosystems. doi: https://doi.org/10.1029/2020GC009322

Arko RC, Chandler P, Clark AM, Mize J (2011) Rolling Deck to Repository (R2R): A, AGU Fall Meeting Abstracts, 03

Batiza R, Vanko D (1984) Petrology of Young Pacific Seamounts. J Geophys Research: Solid Earth 89:11235–11260. https://doi.org/10.1029/JB089iB13p11235

Canales JP, Detrick RS, Toomey DR, Wilcock WSD (2003) Segment scale variations in the crustal structure of 150–300 kyr old fast spreading oceanic crust (East Pacific Rise, 8 150 N–10 150 N) from wide-angle seismic refraction profiles. Geophys J Int 152(3):766–794. https://doi.org/10.1046/j.1365-246X.2003.01885.x

Carbotte S, Macdonald K (1992) East Pacific Rise 8°–10°30′N: Evolution of ridge segments and discontinuities from SeaMARC II and three-dimensional magnetic studies. J Phys Res 97:6959. https://doi.org/10.1029/91jb03065

Carbotte SM, Canales JP, Nedimović MR, Carton H, Mutter JC (2012) Recent Seismic Studies at the East Pacific Rise 8 degrees 20 '-10 degrees 10 ' N and Endeavour Segment Insights into Mid-Ocean Ridge Hydrothermal and Magmatic Processes, Oceanography, 25:100–112

Chen W-P, Molnar P (1983) Focal depths of intracontinental and intraplate earthquakes and their implications for the thermal and mechanical properties of the lithosphere. Journal of Geophysical Research: Solid Earth 88:4183–4214. https://doi.org/10.1029/JB088iB05p04183Chen, Y.J. 1992, Oceanic crustal thickness versus spreading rate: Geophysical Research Letters, v. 19, p. 753–756, https://doi.org/10.1029/92GL00161

Cormier MH, Gans KD, Wilson DS (2011) Gravity lineaments of the Cocos Plate: Evidence for a thermal contraction crack origin. Geochemistry, Geophysics, Geosystems. https://doi.org/10.1029/2011GC003573

DeMets C, Gordon RG, Argus DF, Stein S (2010) Geologically current plate motions. Geophysical Journal International, Volume 181, Issue 1, April 2010, Pages 1–80, https://doi.org/10.1111/j.1365-246X.2009.04491.x

Fabbrizzi A, Parnell-Turner R, Gregg PM, Fornari DJ, Perfit MR, Wanless D, Anderson M (2022) Relative Timing of Off-axis Volcanism from Sediment Thickness Estimates on the 8°20'N Seamount Chain, East Pacific Rise. Geochemistry, Geophysics, Geosystems, accepted

Fornari DJ, Ryan WBF, Fox PJ, Perfit DJ, Allan MR, Batiza R (1984) (1988). Small-scale heterogeneities in depleted mantle sources: near-ridge seamount lava geochemistry and implications for mid-ocean-ridge magmatic processes. Nature, 331(6156), 511–513. https://doi.org/10.1038/331511a0

Fornari DJ, Gallo DG, Edwards MH, Madsen JA, Perfi MR, Shor AN (1989) Structure and topography of the Siqueiros transform fault system: Evidence for the development of intra-transform spreading centers. Mar Geophys Res 11:263–299. https://doi.org/10.1007/BF00282579

Forsyth DW, Harmon N, Scheirer DS, Duncan RA (2006) Distribution of recent volcanism and the morphology of seamounts and ridges in the GLIMPSE study area: Implications for the lithospheric cracking hypothesis for the origin of intraplate, non-hot spot volcanic chains. J Geophys Research: Solid Earth. https://doi.org/10.1029/2005JB004075. 111:n/a-n/a

Gregg P, Hebert L, Montési L, Katz R, Lin PM, Behn J, Montesi LG (2012) (2007). Spreading rate dependence of gravity anomalies along oceanic transform faults. Nature, 448(7150), 183–187. https://doi.org/10.1038/nature05962

Gregg PM, Behn MD, Lin J, Grove TL (2009) Melt generation, crystallization, and extraction beneath segmented oceanic transform faults. J Geophys Research: Solid Earth 114. https://doi.org/10.1029/2008JB006100

Harmon N, Forsyth DW, Scheirer DS (2006) Analysis of gravity and topography in the GLIMPSE study region: Isostatic compensation and uplift of the Sojourn and Hotu Matua Ridge systems. J Geophys Research: Solid Earth 111. https://doi.org/10.1029/2005JB004071

Hosford A, Tivey M, Matsumoto T et al (2003) Crustal magnetization and accretion at the Southwest Indian Ridge near the Atlantis II fracture zone, 0–25 Ma. J Geophys Research: Solid Earth 108. https://doi.org/10.1029/2001JB000604

Klein EM, Langmuir CH (1987) Global correlations of ocean ridge basalt chemistry with axial depth and crustal thickness. J Geophys Research-Solid Earth Planet 92:8089–8115

Koppers A, Watts A (2010) Intraplate Seamounts as a Window into Deep Earth Processes. Oceanography 23:42–57. https://doi.org/10.5670/oceanog.2010.61

Kuo B-Y, Forsyth DW (1988) Gravity anomalies of the ridge-transform system in the South Atlantic between 31 and 34.5 {\textdegree} S: Upwelling centers and variations in crustal thickness. Mar Geophys Res 10:205–232. https://doi.org/10.1007/BF00310065

Langmuir CH, Forsyth DW (2007) Mantle melting beneath mid-ocean ridges. Oceanography 20:78–89

Leeds AR, Knopoff L, Kausel EG (1974) Variations of Upper Mantle Structure under the Pacific Ocean. Sci v 186:141–143. DOI: https://doi.org/10.1126/science.186.4159.141

Lin J, Phipps Morgan J (1992) The spreading rate dependence of three-dimensional mid-ocean ridge gravity structure. Geophys Res Lett 19:13–16

Lin J, Purdy GM, Schouten H et al (1990) Evidence from gravity data for focused magmatic accretion along the Mid-Atlantic Ridge. Nature 344:627–632. https://doi.org/10.1038/344627a0

Marjanović M, Plessix R, Stopin A, Singh SC (2019b) Elastic versus acoustic 3-D full waveform inversion at the East Pacific Rise 9° 50′ N. Geophys J Int 216(3):1497–1506

Macdonald KC, Miller SP, Huestis SP, Spiess FN (1980) Three-dimensional modeling of a magnetic reversal boundary from inversion of deep-tow measurements. J Geophys Research: Solid Earth 85:3670–3680. https://doi.org/10.1029/JB085iB07p03670

Macdonald KC, Fox PJ, Miller S et al (1992) The East Pacific Rise and its flanks 8–18 {\textdegree} N: History of segmentation, propagation and spreading direction based on SeaMARC II and Sea Beam studies. Mar Geophys Res 14:299–344. https://doi.org/10.1007/BF01203621

McKenzie D, Jackson J, Priestley K (2005) Thermal structure of oceanic and continental lithosphere. Earth Planet Sci Lett 233:337–349. https://doi.org/10.1016/J.EPSL.2005.02.005

McNutt MK (1984) Lithospheric flexure and thermal anomalies, Journal of Geophysical Research: Solid Earth 89 https://doi.org/10.1029/JB089iB13p11180

Minshull TA, Charvis PH (2001) Ocean island densities and models of lithospheric flexure. Geophys J Int 145. https://doi.org/10.1046/j.0956-540x.2001.01422.x

Mittelstaedt E, Soule S, Harpp K, Fornari D, McKee C, Tivey M, Geist D, Kurz MD, Sinton C, Mello C (2012) Multiple expressions of plume-ridge interaction in the Galápagos: Volcanic lineaments and ridge jumps, vol 3. Geochemistry, Geophysics, Geosystems

Mittelstaedt E, Soule S, Harpp K, Fornari D (2014) Variations in Crustal Thickness, Plate Rigidity, and Volcanic Processes Throughout the Northern Galápagos Volcanic Province. The Galápagos: A Natural Laboratory for the Earth Sciences. Geophys Monogr 204:263–284

Niu Y, Batiza R (1993) Chemical variation trends at fast and slow spreading mid-ocean ridges. J Geophys Research: Solid Earth 98:7887–7902. https://doi.org/10.1029/93JB00149

Nishimura CE, Forsyth DW (1989) The anisotropic structure of the upper mantle in the Pacific. Geophys J Int 96. https://doi.org/10.1111/j.1365-246X.1989.tb04446.x

Parmentier EM, Haxby WF (1986) Thermal Stresses in the Oceanic Lithosphere' Evidence From Geoid Anomalies at Fracture Zones. J Phys Res 91:7193–7204. https://doi.org/10.1029/JB091iB07p07193

Parker RL, Huestis SP (1974) The inversion of magnetic anomalies in the presence of topography. J Phys Res 79:1587–1593. https://doi.org/10.1029/JB079i011p01587

Parker RL (1974) A new method for modeling marine gravity and magnetic anomalies. J Phys Res 79:2014–2016. https://doi.org/10.1029/JB079i014p02014

Parson B, Sclater JG (1977) An analysis of the variation of ocean floor bathymetry and heat flow with age. J Phys Res 1896–1977. https://doi.org/10.1029/JB082i005p00803

Perfit MR, Fornari DJ, Ridley WI et al (1996) Recent volcanism in the Siqueiros transform fault: picritic basalts and implications for MORB magma genesis. Earth Planet Sci Lett 141:91–108. https://doi.org/10.1016/0012-821X(96)00052-0

Perfit MR, Chadwick WW (1998) Magmatism at mid-ocean ridges: Constraints from volcanological and geochemical investigations. In: Geophysical Monograph Series. pp59–115

Perram LJ, Macdonald KC (1990) A one-million-year history of the 11°45′N East Pacific Rise discontinuity. J Phys Res. 95 https://doi.org/10.1029/JB095iB13p21363

Pockalny R, Fox J, KCM (1991) Generation of volcanic transverse ridge along the Siqueiros fracture zone. Eos Trans AGU Fall Meet Suppl, p 491

Pockalny RA, Fox PJ, Fornari DJ et al (1997) Tectonic reconstruction of the Clipperton and Siqueiros Fracture Zones: Evidence and consequences of plate motion change for the last 3 Myr. J Geophys Research: Solid Earth 102:3167–3181. https://doi.org/10.1029/96JB03391

Sandwell D, Fialko Y (2004) Warping and cracking of the Pacific plate by thermal contraction. J Geophys Res 109. https://doi.org/10.1029/2004JB003091

Sandwell D, Schubert G (1982) Lithospheric flexure at fracture zones. J Geophys Research: Solid Earth 87:4657–4667. https://doi.org/10.1029/JB087iB06p04657

Sandwell DT (1984) Thermomechanical evolution of oceanic fracture zones. J Geophys Research: Solid Earth 89:11401–11413. https://doi.org/10.1029/JB089iB13p11401

Scheirer DS, Macdonald KC (1995) Near-axis seamounts on the flanks of the East Pacific Rise, 8°N to 17°N. J Geophys Research: Solid Earth 100:2239–2259. https://doi.org/10.1029/94JB02769

Searle RC, Escartín J (2004) The Rheology and Morphology of Oceanic Lithosphere and Mid-Ocean, in Mid Ocean Ridges. Hydrothermal interactions between the lithosphere and the oceans, 148, American Geophysical Union, 63:93 Geophysical Monograph Series

Shen Y, Forsyth DW, Scheirer DS, Macdonald KC (1993) Two forms of volcanism: Implications for mantle flow and off-axis crustal production on the west flank of the southern East Pacific Rise. J Geophys Research: Solid Earth 98:17875–17889. https://doi.org/10.1029/93JB01721

Stein CA, Stein S (1992) A Model for the Global Variation in Oceanic Depth and Heat-Flow with Lithospheric Age. Nature 359:123–129

Thébault E, Finlay CC, Alken P et al (2015) Evaluation of candidate geomagnetic field models for IGRF-12. Earth Planet 67. https://doi.org/10.1186/s40623-015-0273-4

Tivey MA, Johnson HP (1990) The magnetic structure of Axial Seamount, Juan de Fuca Ridge. J Phys Res 95. https://doi.org/10.1029/JB095iB08p12735

Tivey MA (1994) Fine-scale magnetic anomaly field over the southern Juan de Fuca Ridge: Axial magnetization low and implications for crustal structure. J Geophys Research: Solid Earth 99:4833–4855. https://doi.org/10.1029/93JB02110

Watts AB (1978) An analysis of isostasy in the world's oceans 1. Hawaiian-Emperor Seamount Chain. J Geophys Research: Solid Earth 83:5989–6004. https://doi.org/10.1029/JB083iB12p05989

Watts AB, Anthony B (2001) Isostasy and flexure of the lithosphere. Cambridge University Press

Wessel P, Haxby WF (1990) Thermal stresses, differential subsidence, and flexure at oceanic fracture zones. J Phys Res 95:375. https://doi.org/10.1029/JB095iB01p00375

Wiens DA, Stein S (1983) Age dependence of oceanic intraplate seismicity and implications for lithospheric evolution. J Phys Res 88:6455. https://doi.org/10.1029/JB088iB08p06455

Williams CM (2007) Oceanic lithosphere magnetization: marine magnetic investigations of crustal accretion and tectonic processes in mid-ocean ridge environments. Massachusetts Institute of Technology and Woods Hole Oceanographic Institution, Woods Hole, MA